PAN

Opto-Electronics Review

journal homepage: https://journals.pan.pl/opelre

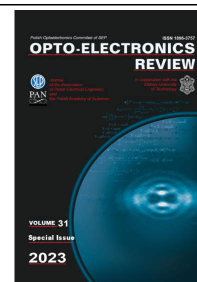

# High performance type-II InAs/GaSb superlattice infrared photodetectors with a short cut-off wavelength

Marie Delmas[1*], David Ramos[1,2], Ruslan Ivanov[1], Laura Žurauskaitė[1], Dean Evans[1], David Rihtnesberg[1], Susanne Almqvist[1], Smilja Becanovic[1], Eric Costard[1], Linda Höglund[1]

[1] IRnova AB, Isafjordsgatan 22, Kista 164 40, Sweden

[2] School of Electrical Engineering and Computer Science KTH Royal Institute of Technology, Isafjordsgatan 22, Kista 164 40, Sweden

**Article info**

*Article history:*
Received 11 Oct. 2022
Received in revised form 30 Nov. 2022
Accepted 30 Dec. 2022
Available on-line 24 Feb. 2023

*Keywords*:
Infrared detectors; short-wavelength infrared; InAs/GaSb superlattice; type-II superlattice.

**Abstract**

This work investigates the potential of InAs/GaSb superlattice detectors for the short-wavelength infrared spectral band. A barrier detector structure was grown by molecular beam epitaxy and devices were fabricated using standard photolithography techniques. Optical and electrical characterisations were carried out and the current limitations were identified. The authors found that the short diffusion length of ~1.8 µm is currently limiting the quantum efficiency (double-pass, no anti-reflection coating) to 43% at 2.8 µm and 200 K. The dark current density is limited by the surface leakage current which shows generation-recombination and diffusion characters below and above 195 K, respectively. By fitting the size dependence of the dark current, the bulk values have been estimated to be $6.57 \cdot 10^{-6}$ A/cm$^2$ at 200 K and $2.31 \cdot 10^{-6}$ A/cm$^2$ at 250 K, which is only a factor of 4 and 2, respectively, above the Rule07.

## 1. Introduction

The short-wavelength infrared (SWIR) spectral region of 1–3 µm is of great interest for a variety of applications such as night vision and long-range identification [1], waste sorting [2], estimation of crop water stress [3], and monitoring volcano activity [4]. Today, the two main technologies for SWIR detection that are used for such applications are $In_xGa_{1-x}As$ and HgCdTe detectors. InGaAs detectors are excellent in terms of uniformity and manufacturability, however, they suffer from a limited cut-off wavelength tunability (to 1.7 µm for lattice-matched $In_{0.53}Ga_{0.47}As$ on InP). Several approaches have been investigated to extend the cut-off wavelength of the InGaAs alloy, for instance, by using appropriate buffer layers when grown on InP substrates [5, 6] or by growing InGaAsSb alloys lattice-matched to GaSb substrates [5, 7, 8]. However, due to mismatch-induced defects, extended InGaAs detectors show increased dark current density and poor uniformity [9], and while InGaAsSb devices have lower dark current than extended InGaAs [5], being a quaternary alloy, InGaAsSb may be more challenging to grow, and it is also known to have a miscibility gap constraining the range of indium composition [10]. HgCdTe, on the other hand, is flexible in terms of a cut-off wavelength but, is rather costly to produce due to the lack of inexpensive substrate and low yield.

In recent years, type-II superlattice (T2SL) photodetectors have demonstrated numerous advantages for infrared detection in the mid-wavelength infrared (MWIR), 3–5 µm spectral band with high performance [11, 12], high uniformity [13], and easy manufacturability [14]. Thanks to great flexibility of the cut-off wavelength, T2SL has also been demonstrated in the SWIR range using Al-based superlattices (SLs), such as InAs/AlSb/GaSb/InAs SL [9, 15–17], InAs/AlAs/InAsSb SL [18], InAs/AlSb SL [19–21], as well as ternary-ternary InGaAs/GaAsSb SL [22, 23]. On the other hand, a very limited number of studies and device performances have been reported for SWIR InAs/GaSb SL, although it has been proven that this material system can reach the cut-off wavelength between 2 and 3 µm by reducing the InAs layer thickness [24–27].

This paper, therefore, aims to evaluate the potential of the InAs/GaSb T2SL for SWIR detection and identify the

*Corresponding author at: marie.delmas@ir-nova.se

https://doi.org/10.24425/opelre.2023.144555
1896-3757/ Association of Polish Electrical Engineers (SEP) and Polish Academic of Sciences (PAS). Published by PAS
© 2023 The Author(s). This is an open access article under the CC BY license (http://creativecommons.org/licenses/by/4.0/).

current limitations. The detector design is based on the IRnova's well-established design for MWIR T2SL detectors presented in Ref. 28 with only small adjustments made to the composition of the T2SL layers to change the cut-off wavelength from ~5.1 µm at 110 K to ~3.5 µm at 150 K as the authors' first demonstration of T2SL detectors with a short cut-off wavelength.

## 2. Experimental details

The detector structure used in this work is based on a so-called barrier detector design, similar to what has already been presented elsewhere [28]. In such device, a large band gap material (referred to as a barrier layer) is inserted between the absorber and the contact regions to block the majority carriers while allowing the unimpeded transport of the photo-generated minority carriers. As long as the electric field is confined in the barrier layer, the generation-recombination (GR) current is suppressed in the absorber region. The dark current is thus diffusion-limited whatever the temperature and it is lower than that of the traditional pin photodiode allowing the device to be operated at higher temperature.

The T2SL detector structure studied in this work was grown on a Te-doped GaSb wafers by molecular beam epitaxy and consists of a contact layer and a barrier layer which are both composed of InAs/AlSb/GaSb/AlSb SL followed by a 3.9 µm thick absorber layer made of a p-type InAs/GaSb SL with a period thickness of 5.6 nm (Fig. 1). The predicted cut-off wavelength calculated using eight band **k·p** simulations is 3.5 µm at 150 K [29]. In the case of a p-type absorber, i.e., electrons are the minority carriers, it is crucial that the conduction band offset between the barrier layer and the absorber layer is close to zero so as not to impede the transport to the contact of the photo-generated electrons. According to the authors' simulations, the conduction band offset is around 7 meV for the chosen T2SL periods. Finally, an appropriate contact layer was grown on top of the structure.

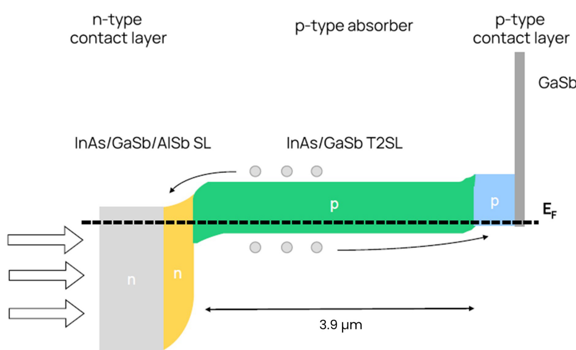


**Fig. 1.** Energy band diagram of the detector structure.

Before the device fabrication, transmission measurements using a Fourier transform infrared spectrometer were done directly on the epi-material on a dedicated sample. One side has been completely etched away to evaluate transmission through the substrate. Devices were then fabricated on the rest of the wafer using standard III/V processing techniques. Fully reticulated diodes were obtained by dry etching down to the bottom contact and were passivated by depositing a dielectric material. Optical characterisations were carried out on a small detector array hybridized to a fan-out chip (silicon chip with a surface metallic pattern mimicking that of a read out integrated circuit). The quantum efficiency (QE) was measured using a dispersive spectrometer with a calibrated photon flux entering through the back side of the structure, and a lock in amplifier was used to suppress the noise and background signal. Note that, the GaSb substrate was removed but no anti-reflection coating was deposited. The dark current measurements were performed with an electrometer on single devices with sizes ranging from 10 µm to 73 µm. In this case, individual devices were directly wire bonded to metal pads.

## 3. Optical characterisations

The measured absorption coefficient corrected for the substrate transmission is plotted in Fig. 2. At 2.8 µm, the absorption coefficient is around 4280 cm$^{-1}$ and 5310 cm$^{-1}$ at 80 K and 300 K, respectively. The 100% cut-off wavelength increases from 3.4 µm to 4 µm when the temperature increases from 80 K to 300 K.

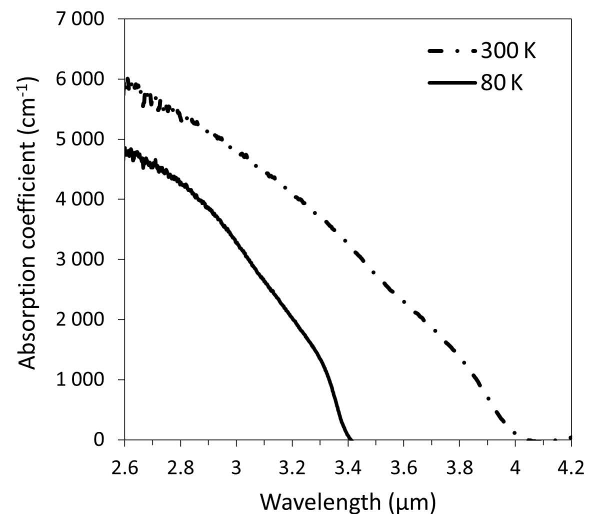


**Fig. 2.** Absorption coefficient at 80 K and 300 K.

In Fig. 3, the QE spectrum measured at a bias of −0.6 V for temperatures ranging from 90 K to 200 K is reported, along with the corresponding QE at a wavelength of 2.8 µm measured as a function of the applied bias. Whilst the choice of plotting the QE at this specific wavelength (2.8 µm) is arbitrary for the figure, the choice of plotting the QE spectra at −0.6 V is not. Indeed, at this bias point, the device is already turned on for all temperatures in the range of 90 K – 200 K. The authors consider that a detector device is turned on when its QE reaches 90% of the QE saturation plateau. At 90 K, the QE is ~31% at −0.6 V, while the QE plateau of the detector is ~35%. For higher temperatures, the QE saturation plateau is already reached at −0.6 V. In addition, the spectrometer being limited to 2.6 µm, the QE at shorter wavelength could not be measured. The 50% cut-off wavelength extracted from the second derivative of the QE spectrum is plotted in the inset of Fig. 3(a). The cut-off wavelength (energy band gap $E_g$) is increasing (decreasing) from ~3.37 µm ($E_g$~0.368 eV) at 90 K to ~3.64 µm ($E_g$~0.341 eV) at 200 K. The temperature dependence of the energy band gap can be well

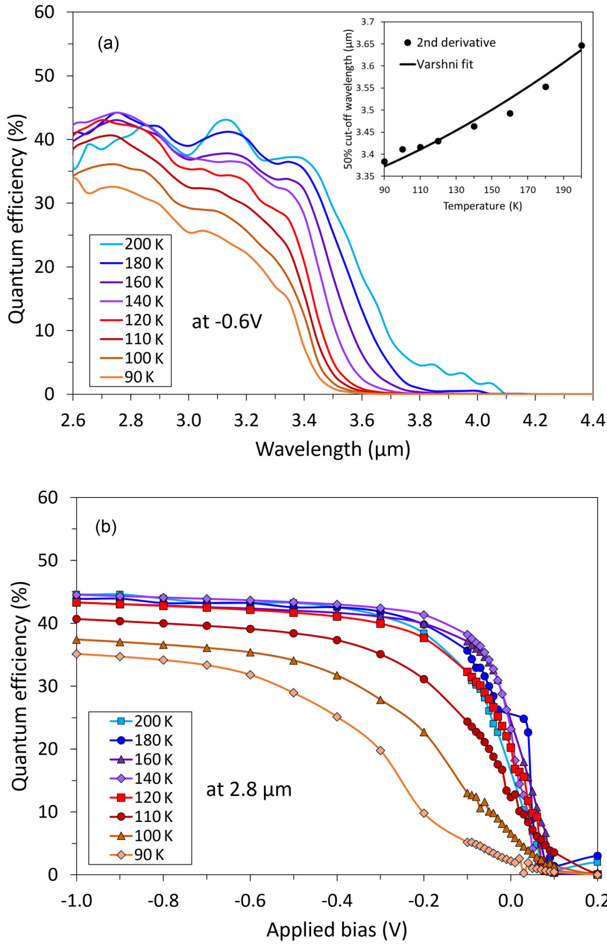


**Fig. 3.** QE spectra measured at −0.6 V at different temperatures (a). QE at a wavelength of 2.8 µm measured as a function of the applied bias at different temperatures (b).

described using the empirical linear-quadratic relation proposed by Varshni [30] with the following parameters: $E_g(0\ \text{K}) = 0.378$ eV, $\alpha = 3.7 \cdot 10^{-4}$ eV/K and $\beta = 200$ K. From Fig. 3(b), it can be seen that the device is fully turned on, i.e., reaches 90% of the saturation, for a bias of −0.5 V at 90 K. This indicates the presence of a barrier in the conduction band at the interface between the absorber and barrier layers, preventing the transport of the photo-generated electrons. The barrier height was estimated to be around 40 meV using similar method employed in Ref. 31. With increasing temperature, the turn on bias required to overcome the electron-blocking barrier decreases to −0.2 V at 200 K. The QE is also temperature-dependent up to 120 K, indeed at −0.6 V and 2.8 µm, it increases from ~32% at 90 K to ~43% at 120 K. This behaviour is attributed to a short diffusion length (inferior to the absorber thickness) of the minority carriers which varies with temperature up to 120 K.

To estimate the electron diffusion length, the authors fitted the experimental QE of Fig. 3 using the well-known Hovel's expressions [32]. This method is often used to estimate the diffusion length in T2SL detectors [33–35]. The total QE can be estimated by calculating the contributions of different parts of the device, namely the neutral region and the depletion region. The model is one-dimensional, and the intensity of the photons varies as $\exp(-\alpha x)$ with $\alpha$ – the absorption coefficient and $x$ – the position in the device. Note that the perfect reflection of the light at the top metal contact is assumed to account for the double-pass configuration. The main input parameters of the simulation are the energy band gap and the absorption coefficient which were both measured. The fitting parameters are the electron diffusion length $L_\mathrm{d}$ which is associated with the vertical transport and the absorber doping concentration $N_\mathrm{dop}$ which governs the depletion width in the absorber as $W = \sqrt{2\varepsilon(V_{on} - V)/(qN_{dop})}$ with $\varepsilon$ – the material permittivity, $q$ – the electron charge, $V_{on}$ – the reverse bias at which the electron-blocking barrier in the conduction band is overcome, and $V$ – the applied bias. Since there is no anti-reflection coating, the authors accounted for ~30% reflection of the incident light at the air/semiconductor interface in the modelling. The fitting results of the QE spectra and its bias dependence are shown in Fig. 4 at a temperature of 120 K. Very good agreement between the measured and calculated QE was obtained for an absorber doping concentration of $N_{dop}$~$1 \cdot 10^{16}$ cm$^{-3}$ and an electron diffusion length of 1.8 µm.

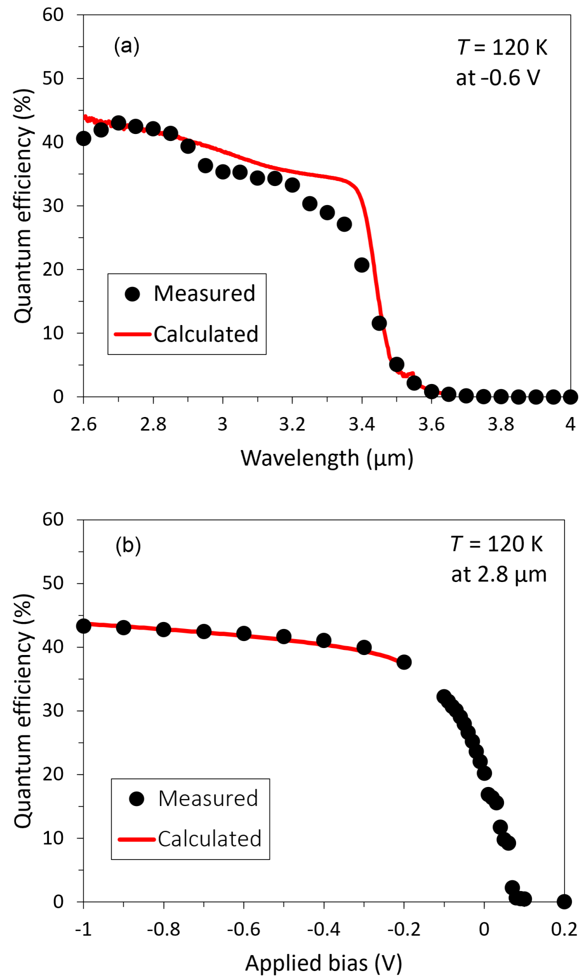


**Fig. 4.** Measured (dots) and calculated QE (solid red line) at a bias of −0.6 V (a), and a wavelength of 2.8 µm at a temperature of 120 K (b).

Similar calculations were performed at different temperatures by keeping the same value of the absorber doping concentration and by adjusting the diffusion length. The extracted diffusion length $L_\mathrm{d}$ of the minority electrons as a function of temperature is reported in Fig. 5. It

increases from 1.4 µm at 90 K to 1.95 µm at 130 K and, from this temperature, it decreases slowly to reach 1.7 µm at 200 K. The diffusion length obtained is quite short considering that the Auger coefficient in InAs/GaSb SL is low in the range of $5\cdot10^{-28}$–$1\cdot10^{-27}$ cm$^6$/s [36, 37], so the Auger recombination should not degrade the lifetime at the absorber doping concentration of the device studied in this work. To better understand the behaviour of the diffusion length, it has been fitted using an expression in the form of $AT^{\alpha}$ with $A$ and α – the constants, and $T$ – the temperature. It is found that the diffusion length is proportional to $T^{-1.275}$ at low temperature and to $T^{-0.262}$ at high temperature. These trends closely follow the trend of the mobility µ when limited by ionized impurity usually dominant at low temperature (µ ∝ $T^{3/2}$ so $L_d \propto T^{5/4}$) and phonon (lattice) scattering usually dominant at high temperature (µ ∝ $T^{-3/2}$ so $L_d \propto T^{-1/4}$). This result demonstrates that the diffusion length is mainly governed by the mobility which is, in part, degraded by an increased number of ionized impurity centre caused by a high doping concentration of the absorber. Therefore, by lowering the absorber doping level, the electron diffusion length can be improved which will increase the QE.

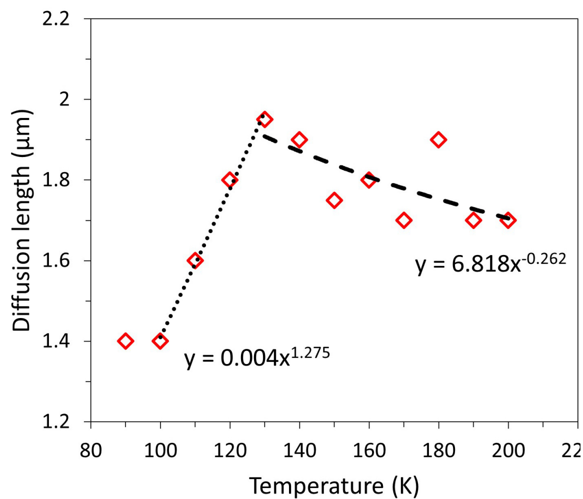


**Fig. 5.** Estimated diffusion length of the minority electrons as a function of temperature (symbols). Low temperature (dotted line) and high temperature (dashed line) trends.

Another or complementary solution to collect all carriers generated would be to reduce the absorber thickness. To determine the optimal thickness for a short diffusion length of 1.8 µm, additional calculations of the QE were carried out at a temperature of 120 K and at a reverse bias of −0.6 V for different absorber thicknesses. The QE value at a wavelength of 2.8 µm is plotted in Fig. 6 as a function of the absorber thickness. The maximum QE of around 50% is reached for an absorber thickness of 1.5 µm, very close to the value of the diffusion length. For a thicker absorber, the QE is decreasing when increasing the absorber thickness due to poor collection, i.e., all photo-generated carriers created recombine before they can be collected. For a thinner absorber, the QE decreases with decreasing absorber thickness due to poor absorption, i.e., the number of photo-generated carriers created and absorbed is limited due to the small absorber volume.

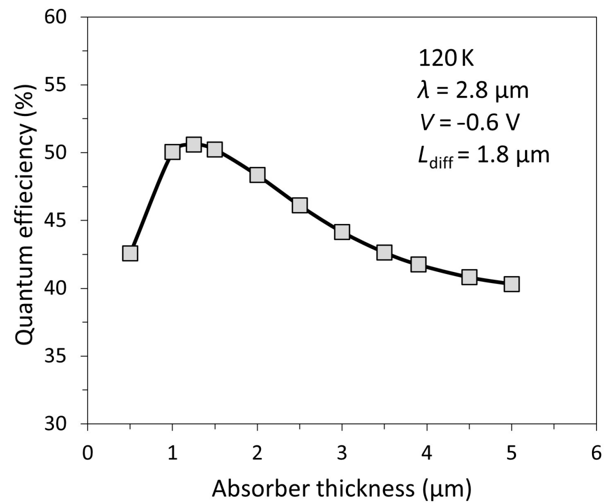


**Fig. 6.** Influence of the absorber thickness on the QE value at −0.6 V and 2.8 µm.

## 4. Dark current measurement

The dark current density measured on a 13 µm device at different temperatures from 150 K to 250 K is plotted in Fig. 7, together with the corresponding variation of the dark current density at −0.6 V. Note that below 150 K, the noise-floor of the electrometer limits the measurement. The dark current density at −0.6 V is $1.1\cdot10^{-4}$ and $6.7\cdot10^{-3}$ A/cm$^2$ at 200 K and 250 K, respectively. The GR and diffusion trends are also plotted in Fig. 7(b). Below ~195 K, the dark current is limited by the GR current with an activation energy of half the band gap, while for temperatures above 195 K, the dark current is diffusion-limited with an activation energy of the full band gap.

To further analyse the dark current, its dependence on the device size was investigated. The total dark current density $J_{\text{tot}}$ in a photodiode is the sum of the bulk current $J_{bulk}$ and the surface component $J_{\text{surf}}$ as $J_{\text{tot}} = J_{\text{bulk}} + J_{\text{surf}} \cdot {}^{P}/_{A}$, with $P$ and $A$ – the perimeter and the area of the device, respectively. In Fig. 8, the dark current density at −0.6 V of different devices with different sizes measured at 200 K and 250 K is plotted as a function of the $P/A$ ratio. Strong size dependence can be observed indicating that the devices are limited by a surface leakage current originating from the mesa sidewalls. In the authors' case, the surface leakage current shows a GR character below 195 K and a diffusion character above this temperature. This behaviour of the surface leakage has recently been studied in Ref. 38 on similar MWIR InAs/GaSb SL detectors. The variation with the device size of the dark current can be fitted with the linear equation using a surface current value of $1.94\cdot10^{-8}$ and $3.47\cdot10^{-8}$ A/cm at 200 K and 250 K, respectively. By improving the fabrication, in particular the passivation, the T2SL detectors presented in this work have the potential to reach a dark current bulk value estimated to be $6.57\cdot10^{-6}$ and $2.31\cdot10^{-6}$ A/cm$^2$ at 200 K and 250 K, respectively. In Fig. 9, the authors compare a measured dark current density of 13 µm mesa (from Fig. 7) to the dark current density of different T2SL detector technologies demonstrated for SWIR detection. These dark current densities are also compared to the Rule 07, which is the HgCdTe benchmark [39]. The dark current of the

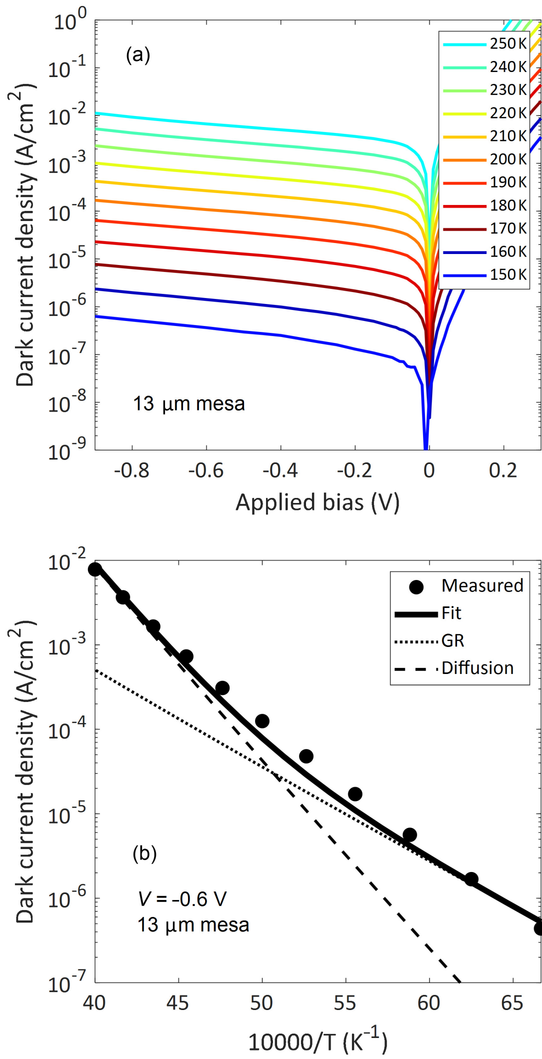


**Fig. 7.** Dark current density of a 13 µm device measured at: different temperatures (a), −0.6 V (dots) as a function of the inverse of the temperature along with the GR (dotted line) and diffusion (dashed line) trends (b). The solid line represents the sum of the GR and diffusion.

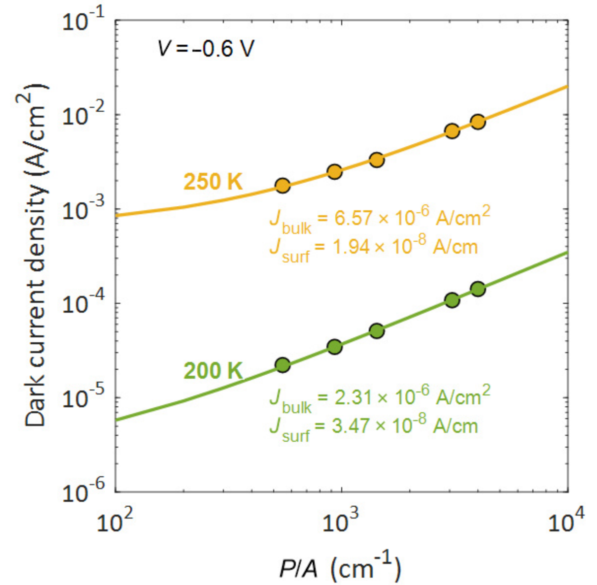


**Fig. 8.** Dark current density measured at −0.6 V (symbols) as a function of the device perimeter over the device area ratio at 200 K (green) and 250 K (yellow). The linear dependence of the dark current density is represented by the solid lines.

13 µm mesa InAs/GaSb SL detector presented in this paper is one of the lowest reported so far and it is a factor of ~200 and ~15 higher than the Rule 07 at 200 K and 250 K, respectively. If the fabrication process is improved and surface leakage is suppressed, the InAs/GaSb SL detector would be the only factor of ~4 and ~2 above the Rule 07 at 200 K and 250 K, respectively. These results demonstrate a strong potential of using T2SL based on InAs/GaSb SL for SWIR detection.

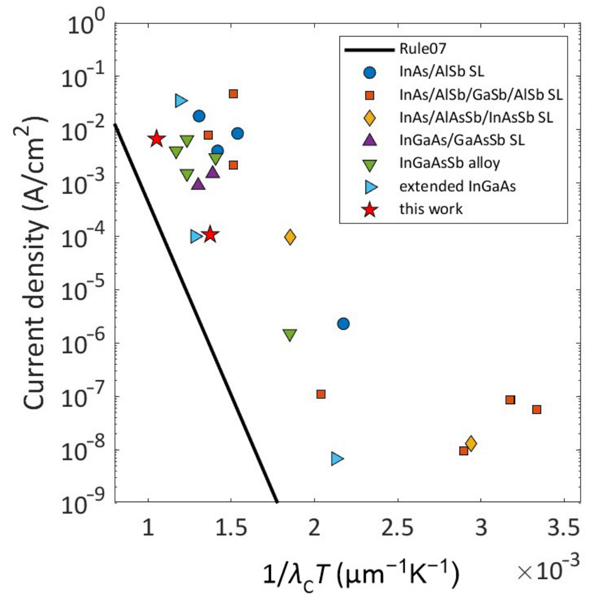


**Fig. 9.** State-of-the-art in terms of dark current density of different T2SL detector technologies for SWIR: InAs/AlSb SL [19–21], InAs/AlSb/GaSb/AlSb SL [9, 15–17], InAs/AlAsSb/InAsSb SL [18], InGaAs/GaAsSb SL [22, 23], InGaAsSb alloy [5, 7, 8] and extended InGaAs [5, 6, 9], and comparison with the Rule07 [39] (black line). Comparison with the dark current of the InAs/GaSb SL detector of this work measured on the 13 µm mesa (red-filled stars).

## 5. Conclusions

In this paper, the authors report on the optical and electrical characterisations of InAs/GaSb SL barrier detectors with a cut-off wavelength of ~3.5 µm (~3.64 µm) at 150 K (200 K). The QE measured in a double-pass configuration and without anti-reflection coating is around 43% at −0.6 V and 200 K. In addition, by fitting the QE and its bias dependence at different temperatures, the authors extracted an electron diffusion length of 1.4 µm at 90 K which increases to ~1.8 µm in the 120 K–200 K temperature range. The short diffusion length is attributed to a degradation of the minority carrier lifetime due to the high doping level of the absorber layer. The dark current density measured on a 13 µm mesa at −0.6 V is $1.1\cdot10^{-4}$ and $6.7\cdot10^{-3}$ A/cm² at 200 K and 250 K, respectively. Surface leakage current was identified as a limiting mechanism of the dark current density. By fitting the size dependence of the dark current, the bulk values have been

estimated to be $6.57\cdot10^{-6}$ A/cm$^2$ at 200 K and $2.31\cdot10^{-6}$ A/cm$^2$ at 250 K, which is only a factor of 4 and 2 above the Rule 07. The results presented in this paper demonstrate the potential of InAs/GaSb SL for SWIR detection.

## References


[1] Driggers R. G., Hodgkin V. & Vollmerhausen, R.. What good is SWIR? Passive day comparison of VIS, NIR, and SWIR. *Proc. SPIE* **8706**, 87060L (2013). https://doi.org/10.1117/12.2016467

[2] Karaca A. C., Ertürk A., Güllü, M. K., Elmas, M. & Ertürk, S. Automatic Waste Sorting Using Shortwave Infrared Hyperspectral Imaging System. in *5th Workshop on Hyperspectral Image and Signal Processing: Evolution in Remote Sensing (WHISPERS)* 1–4 (2013). https://doi.org/10.1109/WHISPERS.2013.8080744

[3] Ghulam A., Li, Z. L., Qin Q., Yimit, H. & Wang J. Estimating crop water stress with ETM+ NIR and SWIR data. *Agric. For. Meteorol.* **148**, 1679–1695 (2008). https://doi.org/10.1016/j.agrformet.2008.05.020

[4] Blackett, M. An overview of infrared remote sensing of volcanic activity. *J. Imaging* **3**, 13 (2017). https://doi.org/10.3390/jimaging3020013

[5] Wicks, G. W. *et al*. Extended-shortwave infrared unipolar barrier detectors. *Proc. SPIE* **9370**, 937023 (2015). https://doi.org/10.1117/12.2083861

[6] Liu, Y. *et al*. High temperature behaviors of 1–2.5 µm extended wavelength In.Ga.As photodetectors on InP substrate. *IEEE J. Quantum Electron.* **57**, 1–7 (2021). https://doi.org/10.1109/JQE.2021.3087324

[7] Prineas, J. P., Yager, J., Seyedmohamadi, S. & Olesberg J. T. Leakage mechanisms and potential performance of molecular-beam epitaxially grown GaInAsSb 2.4 µm photodiode detectors. *J. Appl. Phys.* **103**, 104511 (2008). https://doi.org/10.1063/1.2932080

[8] Craig, A. P. *et al*. Short-wave infrared barriode detectors using InGaAsSb absorption material lattice matched to GaSb. *Appl. Phys. Lett.* **106**, 201103 (2015). https://doi.org/10.1063/1.4921468

[9] Ko, S.-Y. *et al*. Comparison of InGaAs and type-II superlattice-based extended SWIR detectors. *Proc. SPIE* **12107**, 1210703 (2022). https://doi.org/10.1117/12.2607834

[10] Chiu, T. H., Zyskind, J. L. & Tsang, W. T. Molecular beam epitaxial growth of InGaAsSb on (100) GaSb with emission wavelength in the 2 to 2.5 µm range. *J. Electron. Mater*. **16**, 57–61 (1987). https://doi.org/10.1007/BF02667791

[11] Soibel, A. *et al*. Mid-wavelength infrared InAsSb/InAs nBn detectors and FPAs with very low dark current density. *Appl. Phys. Lett*. **114**, 161103 (2019). https://doi.org/10.1063/1.5092342

[12] Delmas, M. *et al*. HOT SWaP and HD detectors based on Type-II superlattices at IRnova. *Proc. SPIE* **12107**, 121070R (2022). https://doi.org/10.1117/12.2618752

[13] Forrai, D. *et al*. Transitioning large-diameter Type II Superlattice detector wafers to manufacturing. *Proc. SPIE* **10624**, 106240L (2018). https://doi.org/10.1117/12.2311515

[14] Höglund, L. *et al*. Manufacturability of type-II InAs/GaSb superlattice detectors for infrared imaging. *Infrared Phys. Technol*. **84**, 28–32 (2017). https://doi.org/10.1016/j.infrared.2017.03.002

[15] Hoang, A. M., Chen, G., Haddadi, A., Abdollahi Pour, S. & Razeghi M. Demonstration of shortwavelength infrared photodiodes based on type-II InAs/GaSb/AlSb superlattices. *Appl. Phys. Lett*. **100**, 211101 (2012). https://doi.org/10.1063/1.4720094

[16] Haddadi, A., Chevallier, R., Dehzangi, A. & Razeghi, M. Extended short-wavelength infrared nBn photodetectors based on type-II InAs/AlSb/GaSb superlattices with an AlAsSb/GaSb superlattice barrier. *Appl. Phys. Lett.* **110**, 101104 (2017). https://doi.org/10.1063/1.4978378

[17] Dehzangi, A., Haddadi, A., Chevallier, R., Zhang,Y. & Razeghi, M. nBn extended short-wavelength infrared focal plane array. *Opt. Lett*. **43**, 591–594 (2018). https://doi.org/10.1364/ol.43.000591

[18] Haddadi, A. *et al*. High-performance short-wavelength infrared photodetectors based on type-II InAs/InAs1-xSbx/AlAs1-xSbx superlattices. *Appl. Phys. Lett*. **107**, 141104 (2015). https://doi.org/10.1063/1.4932518

[19] Cohen-Elias, D. *et al*. Minority carrier diffusion length for electrons in an extended SWIR InAs/AlSb type-II superlattice photodiode. *Appl. Phys. Lett.* **111**, 201106 (2017). https://doi.org/10.1063/1.5005097

[20] Cohen-Elias, D. *et al*. Short wavelength infrared InAs/InSb/AlSb type-II superlattice photodetector. *Infrared Phys. Technol*. **84**, 82–86 (2017). https://doi.org/10.1016/j.infrared.2017.01.005

[21] Shafir, I. *et al*. Improved performances InAs/AlSb Type-II superlattice photodiodes for eSWIR with Ldiff of 2.4 µm and QE of 38% at 300 K. *Infrared Phys. Technol.* **105**, 103210 (2020). https://doi.org/10.1016/j.infrared.2020.103210

[22] Uliel, Y. *et al*. InGaAs/GaAsSb type-II superlattice based photodiodes for short wave infrared detection. *Infrared Phys. Technol.* **84**, 63–71 (2017). https://doi.org/10.1016/j.infrared.2017.02.003

[23] Sugimura, K. *et al*. High-performance extended SWIR photodetectors using strain compensated InGaAs/GaAsSb type-II quantum wells. *Proc. SPIE* **10926**, 109260E (2019). https://doi.org/10.1117/12.2509148

[24] Guo, J. *et al*. InAs/GaSb superlattices for photodetection in short wavelength infrared range. *Infrared Phys. Technol.* **52**, 124–126 (2009). https://doi.org/10.1016/j.infrared.2009.04.003

[25] Gautam, N. *et al*. Three color infrared detector using InAs/GaSb superlattices with unipolar barriers. *Appl. Phys. Lett.* **98**, 121106 (2011). https://doi.org/10.1063/1.3570687

[26] Huang, J. *et al*. How to use type II InAs/GaSb superlattice structure to reach detection wavelength of 2–3 µm. *IEEE J. Quantum Electron.* **48**, 1322–1326 (2012). https://doi.org/10.1109/JQE.2012.2210390

[27] Chen, Y. *et al*. MOCVD growth of InAs/GaSb type-II superlattices on InAs substrates for short wavelength infrared detection. *Infrared Phys. Technol.* **105**, 103209 (2020). https://doi.org/10.1016/j.infrared.2020.103209

[28] Höglund, L. *et al*. Advantages of T2SL: results from production and new development at IRnova. *Proc. SPIE* **9819**, 98190Z (2016). https://doi.org/10.1117/12.2227466

[29] Asplund, C., Marcks von Würtemberg, R. & Höglund, L. Modeling tools for design of type-II superlattice photodetectors. *Infrared Phys. Technol.* **84**, 21–27 (2017). https://doi.org/10.1016/j.infrared.2017.03.006

[30] Varshni, Y. P. Temperature dependence of the energy gap in semiconductors. *Physica* **34**, 149–154 (1967). https://doi.org/10.1016/0031-8914(67)90062-6

[31] Rhiger, D. R. & Smith, E. P. Carrier Transport in the valence band of nBn III–V superlattice infrared detectors. *J. Electron. Mater.* **48**, 6053–6062 (2019). https://doi.org/10.1007/s11664-019-07319-y

[32] Hovel, H. J., Willardson, R. K. & Beer, A. C. *Semiconductors and Semimetals. Vol. 11, Solar Cells* (Academic Press, New York, 1975).

[33] Giard, E., Ribet-Mohamed, I., Delmas, M., Rodriguez, J. B. & Christol, P. Influence of the p-type doping on the radiometric performances of MWIR InAs/GaSb superlattice photodiodes. *Infrared Phys. Technol.* **70**, 103–106 (2015). https://doi.org/10.1016/j.infrared.2014.07.034

[34] Soibel, A. *et al*. Temperature dependence of diffusion length and mobility in mid-wavelength InAs/InAsSb superlattice infrared detectors. *Appl. Phys. Lett.* **117**, 231103 (2020). https://doi.org/10.1063/5.0027230

[35] Rhiger, D. R. & Smith, E. P. Infrared absorption near the bandgap in the InAs/InAsSb superlattice. *Proc. SPIE* **11503**, 1150305 (2020). https://doi.org/10.1117/12.2569820

[36] Youngdale, E. R., Meyer, J. R., Hoffman, C. A. & Bartoli, F. J. Auger lifetime enhancement in InAs-Ga1-xInxSb superlattices. *Appl. Phys. Lett.* **64**, 3160 (1994). https://doi.org/10.1063/1.111325

[37] Taghipour, Z. *et al.* Temperature-dependent minority-carrier mobility in p-type InAs/GaSb type-II-superlattice photodetectors. *Phys. Rev. Appl*. **11**, 024047(2019). https://doi.org/10.1103/PhysRevApplied.11.024047

[38] Ramos, D. *et al*. Quasi-3-dimensional simulations and experimental validation of surface leakage currents in high operating temperature type-II superlattice infrared detectors. *J. Appl. Phys.* **132**, 204501 (2022). https://doi.org/10.1063/5.0106878

[39] Tennant, W. E. "Rule 07" revisited: Still a good heuristic predictor of p/n HgCdTe photodiode performance? *J. Electron. Mater.* **39**, 1030–1035 (2010). https://doi.org/10.1007/s11664-010-1084-9